photonics

MDPI

Article

Detection Capability Analysis of Field of View-Gated Optical Imaging System for All-Time Star Sensor

Liang Fang [1,2,3,4,*], Hui Zhang [1,2,3,4], Xin Cheng [1,2], Zhenjie Fan [1,2], Zhiyuan Liao [1,2,3], Qiang Zhang [5] and Rujin Zhao [1,2,3,4]

1 Institute of Optics and Electronics, Chinese Academy of Sciences, Chengdu 610209, China; hzhang@ioe.ac.cn (H.Z.); chengxin@ioe.ac.cn (X.C.); fanzhenjie@ioe.ac.cn (Z.F.); liao_zy@ioe.ac.cn (Z.L.); zhaorj@ioe.ac.cn (R.Z.)
2 Key Laboratory of Science and Technology on Space Optoelectronic Precision Measurement, Chinese Academy of Sciences, Chengdu 610209, China
3 National Laboratory on Adaptive Optics, Chengdu 610209, China
4 University of Chinese Academy of Sciences, Beijing 100049, China
5 College of Air Traffic Management, Civil Aviation Flight University of China, Guanghan 618307, China; zhangqiangatm@cafuc.edu.cn
* Correspondence: fangl@ioe.ac.cn

Abstract: The field of view (FOV)-gated optical imaging system can relieve the contradiction between a wide FOV and the effective suppression of sky background radiation, making it particularly suitable for all-time star sensors. The detection capability of this novel optical imaging system during daytime differs significantly from that of traditional optical systems. This paper presents the principle of suppressing sky background radiation through FOV-gated imaging. Subsequently, the detection capabilities, including detectable limiting stellar magnitude and the probability of detecting at least three stars, are analyzed for applications on airborne platforms operating at altitudes of no less than 3km. Based on the analysis results, an FOV-gated imaging system operating in the shortwave infrared wavelength band was designed. Additionally, stray light analysis software, ASAP, was employed to simulate the illumination of stellar signals and sky background radiation on the detector. The evaluation of the detection capability of the designed FOV-gated optical system, based on simulation data, aligns with the theoretical analysis value. It demonstrates the system's ability to detect multiple stars with a high probability during the daytime, thereby providing a theoretical foundation for the practical application of the FOV-gated optical imaging system on airborne platforms.

Keywords: all-time star sensor; field of view-gated imaging; detection capability; sky background radiation

check for updates

Citation: Fang, L.; Zhang, H.; Cheng, X.; Fan, Z.; Liao, Z.; Zhang, Q.; Zhao, R. Detection Capability Analysis of Field of View-Gated Optical Imaging System for All-Time Star Sensor. *Photonics* **2024**, *11*, 1118. https://doi.org/10.3390/photonics11121118

Received: 13 October 2024
Revised: 21 November 2024
Accepted: 22 November 2024
Published: 26 November 2024

Copyright: © 2024 by the authors. Licensee MDPI, Basel, Switzerland. This article is an open access article distributed under the terms and conditions of the Creative Commons Attribution (CC BY) license (https://creativecommons.org/licenses/by/4.0/).

1. Introduction

A star sensor is a high-precision instrument utilized for attitude measurement, employing celestial bodies as reference sources. This technology offers several advantages, including high measurement accuracy, robust autonomy, strong resistance to interference, and the absence of time-accumulated errors. Star sensors are predominantly employed in the attitude and orbit control of satellite platforms outside the atmosphere [1–3]. With the rapid advancements in navigation technology, the application of star sensors has progressively expanded from space-based platforms, such as satellites and spacecraft, to airborne platforms, including aircraft and airships. This transition enables airborne platforms to operate independently of satellite navigation systems. Consequently, the development of all-time star sensors has emerged as a critical focus within the field of star sensor technology [4,5].

The primary challenge faced by airborne star sensors is the interference caused by strong background radiation from the sky. To mitigate this background radiation and enhance the signal-to-noise ratio (SNR) of star detection systems, it is common practice

to employ methods such as reducing the FOV and implementing spectral filtering. These techniques are applied in accordance with the different ray directions and spectral characteristics of stellar light in relation to atmospheric background radiation [6–9]. For example, Northrop Grumman Corporation in the United States developed the NAS-26 airborne navigation system, which features an FOV of only 40″. Due to this narrow FOV, the telescope is equipped with a scanning mechanism that allows for a spiral search of the target star [10]. Additionally, Litton Corporation in the United States created the LN-120G astronomical/inertial navigation system. This system utilizes an optical telescope with an enhanced Cassegrain reflection structure, boasting an effective focal length of 347.2 mm, a primary mirror aperture of 95.3 mm, and an FOV of 6′. A single star target is detected within the FOV and is tracked by a mechanical turntable [11]. This type of all-time star sensor, characterized by a narrow FOV, functions primarily as a star tracker and necessitates the integration of a heavy servo system. In 2008, Trex Enterprises in the United States proposed a daytime stellar imager with three large aperture telescopes operating within the shortwave infrared (SWIR) waveband [12]. They claimed that the K-band or H-band shortwave infrared detection system is particularly effective in mitigating sky background light. Furthermore, the utilization of three telescopes enhances the system's detection probability. The horizontal projection angle between the boresights of adjacent FOVs is 120°, while the elevation angle is 45°. Each telescope possesses an FOV of 0.4° × 0.5°. Despite the absence of a mechanical turntable, the daytime stellar imager remains substantial in volume and weight due to the presence of multiple telescopes, posing significant challenges in meeting the operational requirements of airborne platforms. Additionally, the inability to perform multi-star detection with these all-time star sensors precludes the possibility of achieving autonomous celestial navigation.

FOV-gated optical imaging represents an innovative approach for all-time star sensors [13,14]. This technique employs a wide FOV telescope to capture stars and combines narrow instantaneous FOV-gated imaging to effectively mitigate sky background radiation. It is anticipated that this method will facilitate multi-star detection and star pattern recognition during daylight hours. Given the novel imaging modalities, the assessment of its detection capabilities diverges from that of conventional optical systems. This paper presents the principle underlying the suppression of sky background radiation through FOV-gated imaging. Furthermore, the study analyzes the detectable limiting magnitude and the probability of detecting three stars under a typical sky background condition for applications involving airborne platforms operating at altitudes of 3 km and above. Based on the analytical findings, an FOV-gated imaging system operating in the shortwave infrared band is designed, and a numerical simulation is conducted using the stray light analysis software ASAP 2011to validate its detection capabilities.

2. Principle of Suppressing Sky Background Radiation by FOV-Gated Imaging

Figure 1a presents a schematic diagram of an FOV-gated optical imaging system that utilizes a microlens and microshutter array. This system comprises three primary components: a prepositive telescope featuring a telecentric beam path in the image space, a microlens and microshutter array, and a common postpositive imaging lens. The prepositive telescope is characterized by a large aperture, a wide FOV, and a short focal length, enabling it to collect light from multiple stars and form images on the intermediate image plane. The microshutter and microlens array serve to gate a narrow instantaneous FOV of the prepositive telescope. The postpositive imaging lens, in conjunction with the microlens elements, forms a magnifying imaging system that enhances the stellar images on the intermediate image plane. Each microlens element is aligned such that its optical axis is parallel to that of the postpositive imaging lens, resulting in the creation of multiple imaging channels within the system. Through the rapid switching of the gated FOV by the microshutter array, the stellar images on the intermediate image plane can be gated swiftly, allowing the magnified stellar images to be recorded by a common detector. If the

switching frequency is sufficiently high, this system can be regarded as the simultaneous detection of multiple stars within a wide FOV during the daytime.

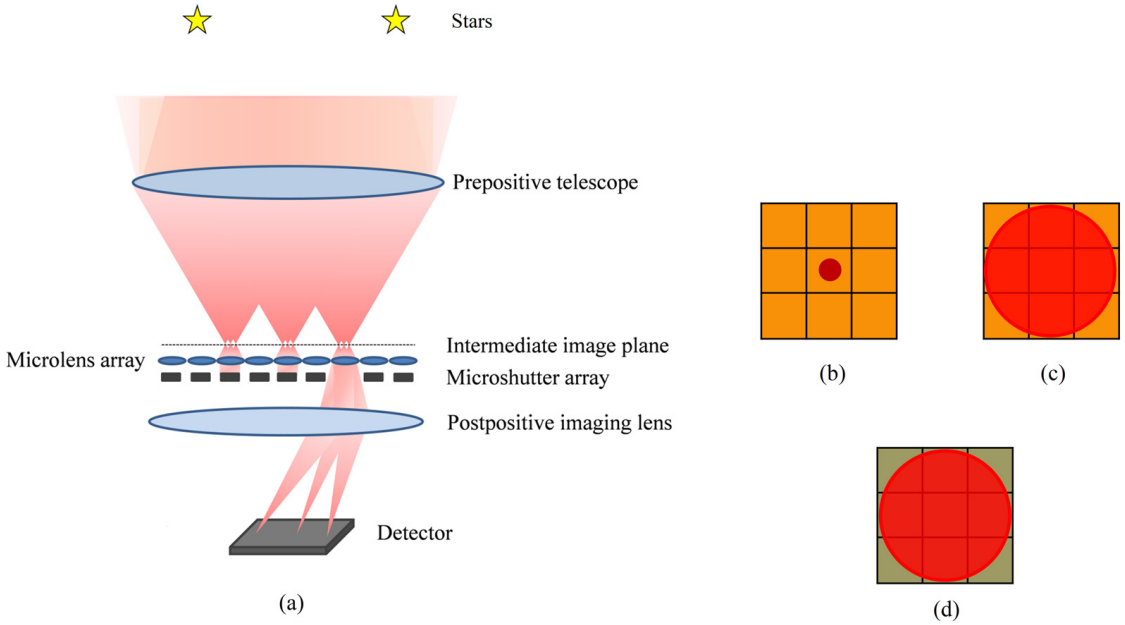


Figure 1. (**a**) Schematic diagram of FOV-gated optical imaging system. (**b**) Stellar image and sky background on the detector positioned at the intermediate image plane. (**c**) Defocused stellar image and sky background on the detector positioned slightly away from the intermediate image plane. (**d**) Stellar image and sky background on the detector positioned at the final image plane.

How to suppress sky background radiation by FOV-gated imaging is an exciting significant problem. This is because the imaging system is not only influenced by imaging quality but is also closely related to the characteristics of the detector. Consequently, to address this issue, it is essential to consider the performance of a detector. The principle of suppressing sky background radiation through field of view (FOV)-gated imaging can be elucidated by comparing the number of electrons generated on the detector as a result of stellar signals and sky background radiation at both the intermediate image plane and the final image plane.

Assuming that an array detector is positioned at the intermediate image plane of the optical system, the stellar image spot may be smaller than the pixel dimensions due to the short focal length of the prepositive telescope, as illustrated in Figure 1b. A small square symbolizes a pixel, while the orange area indicates the sky background radiation. The red disk represents the stellar image, which is distributed within a single pixel.

The total number of electrons generated by the stellar signal within a pixel on the intermediate image plane can be expressed as follows [15]:

$$S_1 = \int_{\lambda_1}^{\lambda_2} F_m(\lambda) T_0(H, \theta_{VZA}, \lambda) \frac{\pi D^2}{4} T_p(\lambda) t \times \frac{Q_0(\lambda)}{h\nu} d\lambda \quad (1)$$

where λ is the operating wavelength; $F_m(\lambda)$ denotes the energy emitted per second per unit area per wavelength from a star with magnitude m at wavelength λ. $T_0(H, \theta_{VZA}, \lambda)$ indicates the atmospheric transmittance as a function of the height H of the star sensor observation position and the view zenith angles θ_{VZA} of the star sensor. D and $T_p(\lambda)$ are the effective aperture and the optical transmittance of the prepositive telescope. t is the exposure time. $h\nu$ is the energy of a single photon, and $Q_0(\lambda)$ indicates the quantum efficiency of the detector. As illustrated in Equation (1), the stellar signal within a pixel is related to the aperture of the telescope but is independent of the FOV of the telescope.

The number of electrons produced by sky background radiation in a pixel located on the intermediate image plane can be expressed as follows:

$$B_1 = \int_{\lambda_1}^{\lambda_2} I_b(\lambda, \theta_{VZA}, \theta_{SZA}, \varphi_{VAA}, H) \frac{\pi D^2}{4} T_p(\lambda) t \times \frac{Q_0(\lambda) \Omega_1}{h\nu} d\lambda \tag{2}$$

where $I_b(\lambda, \theta_{VZA}, \theta_{SZA}, \varphi_{VAA}, H)$ is the sky background radiation intensity with the height H of the star sensor observation position, as well as the view zenith angles θ_{VZA}, solar zenith angles θ_{SZA}, and the view azimuth angle φ_{VAA} of the star sensor. Ω_1 is the solid angle corresponding to a single pixel on the intermediate image plane and can be expressed as follows:

$$\Omega_1 = 2\pi\left(1 - cos\frac{w_{pixel}}{2}\right) = 2\pi\left(1 - cos\frac{w}{2\mathrm{N}_d}\right) = 2\pi\left(1 - cos\frac{d_{pixel}}{2f_p}\right) \tag{3}$$

where w_{pixel} is the single-pixel FOV on the intermediate image plane, w is the FOV of the prepositive telescope, and N_d is the effective pixel number of the detector; w_{pixel} can be expressed as $\frac{w}{\mathrm{N}_d}$ or $\frac{d_{pixel}}{f_p}$, where d_{pixel} is the pixel dimension of the detector, and f_p is the focal length of the prepositive telescope. As can be seen from Equations (2) and (3), the sky background radiation within a pixel is influenced by both the aperture of the telescope and the single-pixel FOV. When N_d is constant, an increase in the FOV of the telescope results in a corresponding increase in the sky background radiation.

From Equations (1)–(3), the ratio of the number of electrons generated by the stellar signal to the number of electrons produced by the sky background radiation in a single pixel on the intermediate image plane is given by

$$R_1 = \frac{S_1}{B_1} = \frac{\int_{\lambda_1}^{\lambda_2} F_m(\lambda) T_0(H, \theta_{VZA}, \lambda) T_p(\lambda) Q_0(\lambda) d\lambda}{\int_{\lambda_1}^{\lambda_2} I_b(\lambda, \theta_{VZA}, \theta_{SZA}, \varphi_{VAA}, H) T_p(\lambda) Q_0(\lambda) \Omega_1 d\lambda} \tag{4}$$

Rather than positioning the detector on the intermediate image plane, the FOV-gated optical imaging system utilizes a gated microlens in conjunction with a postpositive imaging lens to magnify the stellar image within the gated FOV on the intermediate image plane. This system subsequently captures the magnified stellar image using the same detector on the final image plane. The distribution diagram of the magnified stellar image on the detector is illustrated in Figure 1d, where the red disk signifies the magnified stellar image that occupies an $N \times N$ pixel area. The number of electrons generated by the magnified stellar signal within a pixel can be expressed as follows:

$$S_2 = \frac{1}{N^2} \int_{\lambda_1}^{\lambda_2} F_m(\lambda) T_0(H, \theta_{VZA}, \lambda) \frac{\pi D^2}{4} T_w(\lambda) t \times \frac{Q_0(\lambda)}{h\nu} d\lambda \tag{5}$$

$T_w(\lambda)$ is the optical transmittance of the whole optical system. The number of generated electrons B_2 caused by the sky background radiation within a pixel on the final image plane can be expressed as

$$B_2 = \int_{\lambda_1}^{\lambda_2} I_b(\lambda, \theta_{VZA}, \theta_{SZA}, \varphi_{VAA}, H) \frac{\pi D^2}{4} T_w(\lambda) t \times \frac{Q_0(\lambda) \Omega_2}{h\nu} d\lambda \tag{6}$$

where Ω_2 is the solid angle of a single pixel on the final image plane and can be expressed as

$$\Omega_2 = 2\pi\left(1 - cos\frac{w_{Gpixel}}{2}\right) = 2\pi\left(1 - cos\frac{w_G}{2\mathrm{N}_d}\right) = 2\pi\left(1 - cos\frac{d_{pixel}}{2f_w}\right) \tag{7}$$

where w_{Gpixel} is the single-pixel FOV on the final image plane, w_G is the gated FOV, N_d is the effective pixel number of the detector, and f_w is the total focal length of the whole optical system. w_{Gpixel} can be expressed as $\frac{w_G}{N_d}$ or $\frac{d_{pixel}}{2f_w}$. Assuming that the magnification of the magnifying imaging is n, f_w can be written as $f_w = nf_p$.

According to Equations (5)–(7), the ratio of the number of electrons generated by the stellar signal to the number of electrons produced by the sky background radiation in a single pixel on the final image plane is

$$R_2 = \frac{S_2}{B_2} = \frac{\frac{1}{N^2}\int_{\lambda_1}^{\lambda_2} F_m(\lambda)T_0(H,\theta_{VZA},\lambda)T_w(\lambda)Q_0(\lambda)d\lambda}{\int_{\lambda_1}^{\lambda_2} I_b(\lambda,\theta_{VZA},\theta_{SZA},\varphi_{VAA},H)T_w(\lambda)Q_0(\lambda)\Omega_2 d\lambda} \tag{8}$$

As the slight difference between $T_p(\lambda)$ and $T_w(\lambda)$ is negligible, $T_p(\lambda)$ and $T_w(\lambda)$ are regarded as approximately equal. Therefore, from Equations (4) and (8), we can obtain

$$R_{21} = \frac{R_2}{R_1} \approx \frac{1}{N^2}\frac{\Omega_1}{\Omega_2} \approx \frac{1}{N^2}\frac{f_w^2}{f_p^2} = \frac{n^2}{N^2} \tag{9}$$

As indicated in Equation (9), the ratio of the number of electrons generated by the stellar signal to the number of electrons produced by the sky background radiation within a single pixel on the final image plane is n^2/N^2 times that on the intermediate image plane. When n is greater than N, the proportion of the number of electrons generated by the stellar signal within a pixel of the same detector will increase from the intermediate image plane to the final image plane. For instance, if the stellar image only is distributed in a 0.6×0.6 pixel area on the intermediate image plane, following a fivefold magnification, the stellar image will encompass a 3×3 pixel area on the final image plane. In this case, $n = 5$ and $N = 3$. It indicates that the sky background radiation is effectively mitigated within a pixel, thereby enhancing the SNR of the stellar image during daytime observations.

It is noteworthy that it is impractical for the stellar image to be confined to a single pixel on the intermediate image plane in a star sensor. To enhance the accuracy of centroid positioning, the detector should be positioned slightly away from the intermediate image plane. A defocused stellar image will encompass multiple pixels, as illustrated by the red disk in Figure 1c. If the defocused stellar image is also distributed across $N \times N$ pixels, the number of electrons generated by the stellar signal in a pixel adjacent to the intermediate image plane will be

$$S_1' = \frac{1}{N^2}S_1 \tag{10}$$

Although the number of electrons S_1' generated by the defocused stellar image in a pixel adjacent to the intermediate image plane diminishes, the number of electrons B_1' produced by the sky background radiation in a pixel near the intermediate image plane remains relatively constant, so

$$B_1' \approx B_1 \tag{11}$$

In this case, the ratio of the number of electrons generated by the stellar signal to the number of electrons produced by the sky background radiation within a single pixel near the intermediate image plane is

$$R_1' = \frac{S_1'}{B_1'} \approx \frac{1}{N^2}R_1 \tag{12}$$

The defocus mentioned above only affects the number of electrons generated by the stellar signal in a single pixel on the intermediate image plane. The ratio of the number of electrons generated by the stellar signal to the number of electrons produced by the sky

background radiation in a single pixel on the final image plane is still R_2. Correspondingly, the ratio of R_2 to R_1' can be written as

$$R_{21}' = \frac{R_2}{R_1'} \approx \frac{\Omega_1}{\Omega_2} \approx n^2 \tag{13}$$

As can be seen from Equation (13), the ratio of the number of electrons generated by the stellar signal to the number of electrons produced by the sky background radiation in a single pixel on the final image plane is n^2 times that on the intermediate image plane. In this case, the suppression of the sky background radiation by FOV-gated imaging appears to be more pronounced.

The optical system of a conventional star sensor can effectively suppress sky background radiation by employing a long-focal-length design. However, the limited photosensitive area of the detector results in a very narrow FOV, which precludes the possibility of detecting multiple stars within that FOV. In contrast, the FOV-gated optical imaging system utilizes a common detector for the imaging plane of each gated FOV, with only one gated FOV operational at any given time. By rapidly switching between gated FOVs, this system enables the nearly simultaneous observation of all stars within the wide FOV of the prepositive telescope. Consequently, the FOV-gated imaging system facilitates multi-star detection even during daylight hours. Furthermore, the shared detector across each gated FOV confers additional advantages, including reduced cost, compact size, and lightweight design.

3. Detection Capability of an FOV-Gated Optical Imaging System

The detection capabilities of an FOV-gated optical imaging system encompass two primary aspects: the detectable limiting stellar magnitude and the probability of detecting multiple stars. To analyze the detectable magnitude limit and the probability of multi-star detection in an FOV-gated imaging system during daytime conditions, it is essential to first estimate the background radiation of the sky.

3.1. Estimation of Sky Background Radiation

Research studies [16,17] demonstrate that both the intensity of stellar light and atmospheric background light diminish as the wavelength increases, with atmospheric background light exhibiting a more rapid decrease than stellar light. In comparison to a star sensor working in the visible waveband, a star sensor operating in the SWIR range has a significantly higher probability of detecting stars [12]. Therefore, considering the detector's spectral response, we selected the operating wavelength range of 1.3 μm to 1.7 μm.

The stellar signal can be conceptualized as parallel light. The energy received from the star is independent of FOV and is associated with the aperture of the optical system. By consulting the optical manual [18], the spectral irradiance of 0-magnitude stars in the H-band is 1.18×10^{-9} W/m^2·μm. Consequently, the stellar energy received can then be calculated based on the aperture size of the optical system, the spectral bandwidth, and the integration time of the detector.

The calculation of sky background radiation is considerably more complex than that of stellar signals due to the significant influence of various observational conditions, including observation height, observation direction, solar zenith angle, and other relevant parameters. Generally, the sky background radiation under varying observational conditions can be simulated and analyzed using PcModWin 6 software based on the MODTRAN model [19]. For an airborne platform, the observation height is approximately 3 km and above. Figure 2a–c illustrate the relationship between sky background radiation within the wavelength range of 1.3 μm to 1.7 μm and the view azimuth angle (VAA) at different solar zenith angles, with view zenith angles (VZAs) set at 0°, 30°, and 60° when the observation height is 3 km, respectively.

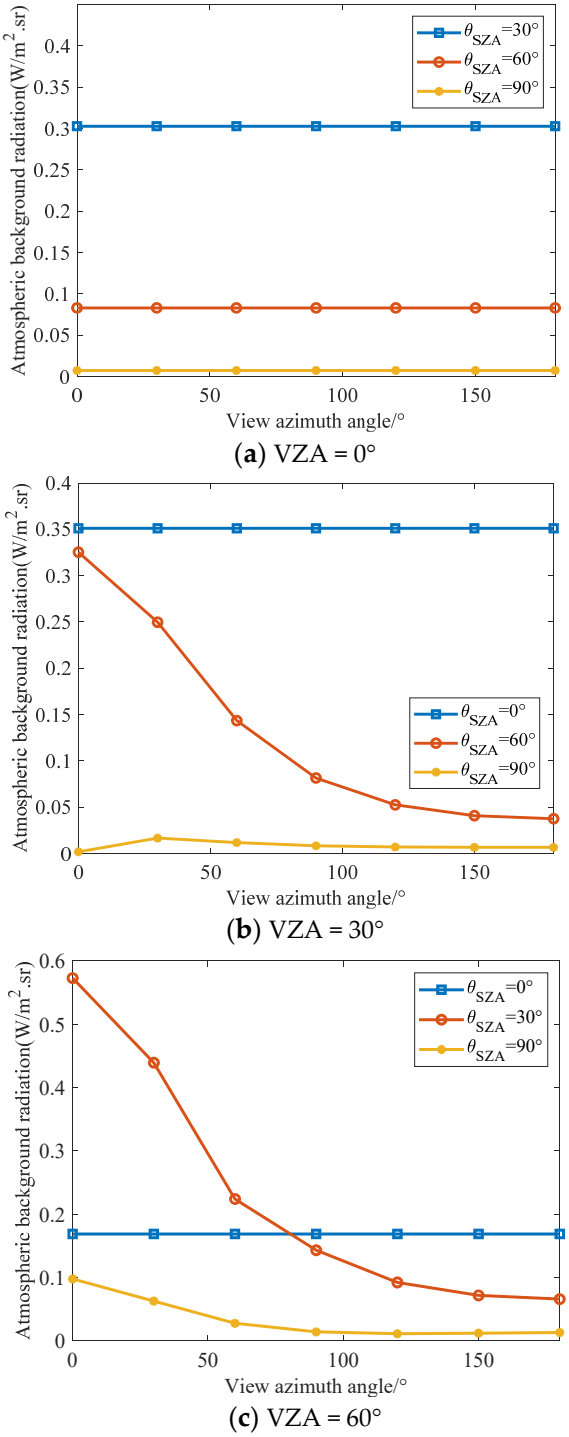


Figure 2. The variation curve of sky background radiation within the waveband of 1.3 μm to 1.7 μm with the view azimuth angle at various solar zenith angles and view zenith angles.

As illustrated in Figure 2, when the angle between the solar direction and the observation direction exceeds 30°, the majority of sky background radiation is observed to be less than 0.35 W/m^2·Sr. Consequently, when the sunlight avoidance angle is set at 30°, a value of 0.35 W/m^2·Sr can be employed as the typical sky background radiance at altitudes of 3 km. This value serves as a conservative estimate for determining the detectable magnitude limit and the likelihood of detecting multiple stars.

Generally, the radiance of the sky background diminishes with increasing altitude. Utilizing the same methodology, a comprehensive analysis of the typical sky background

radiance at various altitudes was conducted. The typical sky background radiance at altitudes of 3 km, 5 km, 8 km, and 10 km is presented in Table 1. Based on the typical sky backgrounds outlined in Table 1, it is possible to estimate the detectable magnitude limit and the probability of detecting multiple stars at different altitudes.

Table 1. The typical sky background radiance at various altitudes during the daytime.

Altitude	3 km	5 km	8 km	10 km
Typical sky background radiance ($W/m^2 \cdot Sr$)	0.35	0.07	0.029	0.019

3.2. Detectable Limiting Stellar Magnitude

The detectable limiting stellar magnitude can be determined by evaluating the SNR of the stellar image, which is closely related to the performance characteristics of the detector. For instance, equipped with the same optical system, a star sensor is capable of detecting stars with a magnitude of 4 in the H-band when paired with an SWIR camera exhibiting a readout noise of 13 electrons, but only can detect stars with a magnitude of 2.3 when an SWIR camera with a readout noise of 150 electrons is used [12]. Therefore, it is imperative to consider the performance of the detector when estimating the detectable limiting stellar magnitude. Assuming a commercial shortwave infrared detector (Bobcat-640-GigE, Xenic Corporation, Santa Clara, CA, USA) is used, its pixel size is $d_{pixel} = 20$ μm and the array format is 640 × 512. The quantum efficiency within the waveband of 1.3 μm to 1.7 μm is 80%, the typical dark current is 1.9×10^5 electrons/s, the readout noise in the high-gain mode is 60 electrons, and the full well capacity is 8×10^4 e^-/pixel.

If the gated FOV is θ_i and the corresponding effective pixel number of the detector is $N_i \times N_i$, the single-pixel FOV can be written as

$$\theta_{pixel} = \theta_i / N_i \tag{14}$$

The total focal length of the whole optical system can be expressed as

$$f_w \approx d_{pixel} / \theta_{pixel} \tag{15}$$

On the other hand, to ensure the concentration of energy and the accuracy of spot position extraction in a stellar image, the diameter d_s of the stellar image on the final image plane should encompass a 3 × 3 pixel area. If the near diffraction limit imaging is achieved, then

$$d_s = 2.44 \frac{\lambda f_w}{D} \leq 3 d_{pixel} \tag{16}$$

According to Equation (16), the effective aperture of the system should satisfy the following expression.

$$D \geq \frac{2.44 \lambda f_w}{3 d_{pixel}} \tag{17}$$

We set the pixel dimension d_{pixel}, the effective pixel number of the detector $N_i \times N_i$, and the operating center wavelength λ as 20 μm, 512 × 512, and 1.5 μm, respectively. Utilizing Equations (14)–(17), the single-pixel FOV θ_{pixel}, the total focal length f_w, and the minimum effective aperture D_{min} of the system can be determined for gated FOV values of 0.2°, 0.3°, 0.4°, 0.5°, 0.6°, and 0.7°, as presented in Table 2.

Table 2. The calculated optical parameters based on various gated FOVs.

Gated FOV	0.2°	0.3°	0.4°	0.5°	0.6°	0.7°
θ_{pixel} (″)	1.41	2.11″	2.81″	3.52″	4.22″	4.92″
f_w (mm)	2935.03	1956.69	1467.52	1174.01	978.34 mm	838.58 mm
D_{min} (mm)	179.04	119.36	89.52	71.61	59.57 mm	51.15 mm

Table 1 indicates that when the gated FOV is less than 0.3°, the system's effective aperture should exceed 120 mm, which is excessively large for an airborne platform. Consequently, only gated FOV values of 0.4°, 0.5°, 0.6°, and 0.7° are taken into account for estimating the detectable magnitude limit.

The detectable magnitude limit can be written as follows [7]:

$$Mv = log_{2.512}\left(\frac{2K_0 \cdot S_0}{SNR^2 + \sqrt{SNR^4 + 4 \cdot SNR^2 \cdot (B + I_{dark} \cdot t + \sigma_{read}^2)}}\right) \tag{18}$$

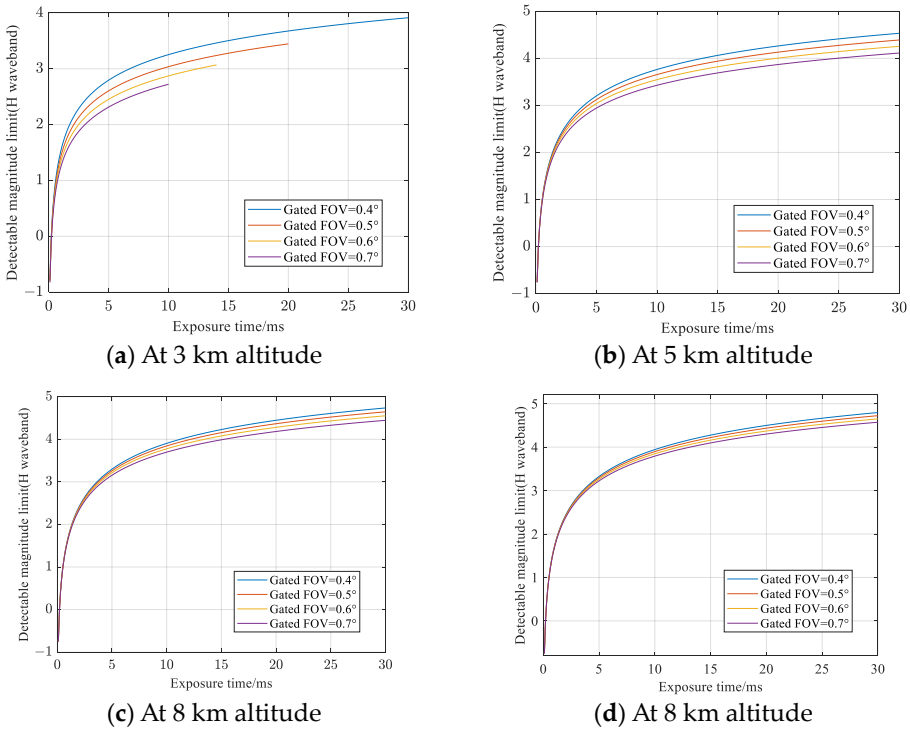
where K_0 is the ratio of the stellar signal energy in a single pixel to the total stellar signal energy, S_0 is the total number of photoelectrons generated by a stellar signal with a magnitude of zero, SNR represents the signal-to-noise ratio threshold for the stellar image on the detector, B is the number of electrons produced by the sky background radiation, I_{dark} is the dark current of the detector, t is the exposure time, and σ_{read} is the readout noise.

It is worth noting that the exposure time of the detector Is constrained by its full well capacity. The cumulative number of photoelectrons generated by the signal light, sky background radiation, and detector noise should not exceed 80% of the full well capacity. Assuming that the full well capacity of the detector is C_{fw}, the maximum exposure time can be expressed as

$$t_{max} = \frac{0.8C_{fw} - \sigma_{read}^2}{S_{mp0} + B_{p0} + I_{dark}} \tag{19}$$

where S_{mp0} and B_{p0} denote the number of photoelectrons generated per second in a single pixel, attributed to m-magnitude stars and the sky background radiation, respectively.

Assuming an aperture diameter of 100 mm for the optical imaging system, with an optical transmittance of 80% and an atmospheric transmittance also at 80%, the SNR threshold is set at greater than 5. The maximum exposure time and the detectable magnitude limit for various gated FOVs at an altitude of 3 km can be calculated, as illustrated in Figure 3a.



(**a**) At 3 km altitude (**b**) At 5 km altitude

(**c**) At 8 km altitude (**d**) At 8 km altitude

Figure 3. The detectable magnitude limit with different exposure times and different gated FOVs at different altitudes.

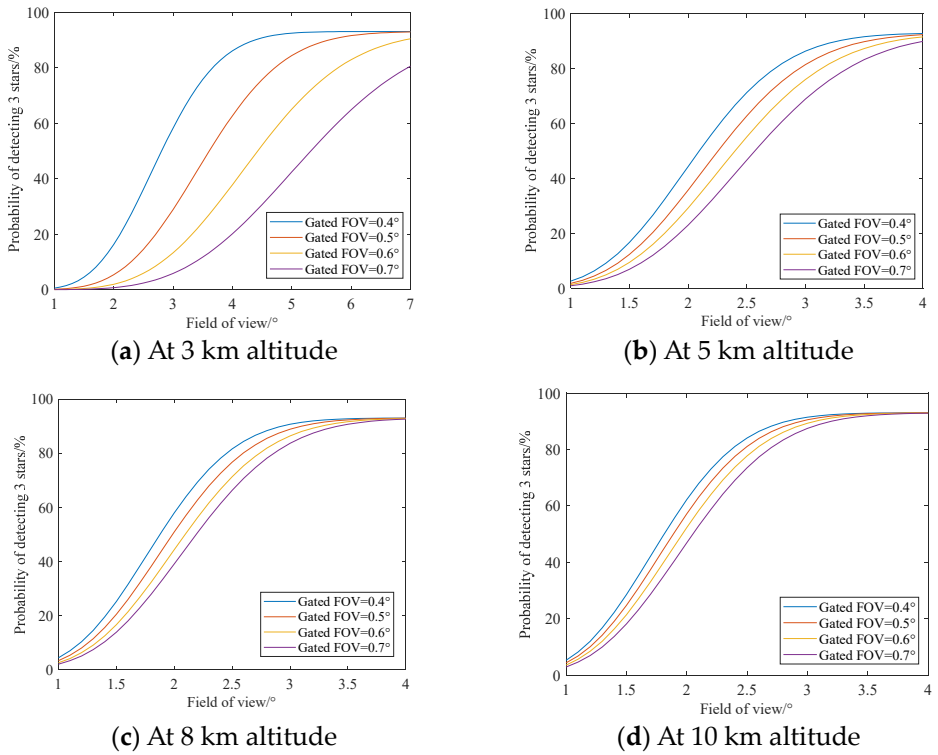
From Figure 3a, the maximum exposure times for gated FOV of 0.4°, 0.5°, 0.6°, and 0.7° are 30 ms, 20 ms, 14 ms, and 10 ms, respectively. Correspondingly, the detectable limiting magnitudes in the H-band are approximately 3.9, 3.4, 3.0, and 2.7, respectively.

As altitude increases, the background radiation of the sky diminishes, resulting in an extended maximum exposure time. According to Formula (19), the maximum exposure time for various gated FOVs exceeds 40 ms at an altitude of 5 km and reaches up to 100 ms at altitudes above 8 km. While it is possible to observe fainter magnitudes, prolonged exposure times may lead to the drift of star spots on an airborne platform. Figure 3b–d illustrate the detectable magnitude limit for different gated FOVs at a maximum exposure time of 30 milliseconds, corresponding to altitudes of 5 km, 8 km, and 10 km, respectively. It is observed that a larger gated FOV correlates with a brighter-detectable-limit magnitude. However, as altitude increases, the impact of the gated FOV on the detectable limit magnitude diminishes. Notably, at altitudes exceeding 5 km, the detectable magnitude limit consistently exceeds the fourth magnitude in the H-band.

In contrast to conventional optical imaging systems, an FOV-gated optical imaging system incorporates two distinct types of FOV: gated FOV and total FOV. The gated FOV primarily influences the detectable magnitude limit, while the total FOV affects the probability of detecting multiple stars. Given that the determination of the platform's attitude necessitates the detection of at least three stars, the subsequent analysis will concentrate on the effects of varying total FOVs and gated FOVs on the detection probability of three stars.

3.3. Probability of Detecting at Least Three Stars

According to the 2MASS catalog and the detectable limiting magnitude in the H-band, the probability of detecting at least three stars with varying gated FOVs and total FOVs at different altitudes is illustrated in Figure 4. It is important to note that due to the sunlight avoidance angle of 30°, a specific region of the sky in the solar neighborhood is inaccessible. Consequently, the maximum detection probability across the entire sky area is approximately 93%.



(**a**) At 3 km altitude (**b**) At 5 km altitude

(**c**) At 8 km altitude (**d**) At 10 km altitude

Figure 4. The probability of detecting at least 3 stars with various total FOVs and gated FOVs at different altitudes.

As illustrated in Figure 4, to achieve an 80% probability of detecting three stars at an altitude of 3 km, the total FOV of the system should exceed 3.8°, 4.8°, 5.8°, and 7° for gated FOV values of 0.4°, 0.5°, 0.6°, and 0.7°, respectively. When the gated FOV is held constant, the required total FOV progressively decreases as altitude increases. Specifically, when the gated FOV is set at 0.4° and the total FOV is 3.8°, a minimum probability of 80% for detecting three stars can be achieved at altitudes of 3 km and above. It is noted that the duty cycle of the FOV cannot reach 100%. Assuming a duty cycle of 0.6 [13], the total FOV should not be less than 6.3°.

4. Designed FOV-Gated Imaging System

Based on the above analysis, an FOV-gated optical imaging system was designed, as illustrated in Figure 5. The operational wavelength range of the imaging system spans from 1.3 μm to 1.7 μm. The specifications of the prepositive telescope include an aperture of 100 mm, a focal length of 300.83 mm, and an FOV of 7°. To enhance design flexibility for optimizing imaging quality and to improve the duty cycle of the FOV, a microlens array comprising both a front microlens array and a rear microlens array was developed. Each microlens features an aperture of 3.5 mm, with a focal length for the microlens group of 9.14 mm, resulting in a gated FOV of 0.4° for each microlens group. The aperture of the postpositive imaging lens measures approximately 41.92 mm, with a focal length of 45.25 mm. The combination of the microlens group and the postpositive imaging lens yields a magnified imaging system with a magnification factor of 4.95. Additionally, the microshutter array is positioned 2 mm behind the microlens array group, with each microshutter element also having an aperture of 3.5 mm. The total focal length of the entire optical system is 1489 mm. The principal parameters of each optical element within this optical imaging system are detailed in Table 3. Notably, the conic constant of the 28th surface is −0.6114, while the coefficients for the 4th-, 6th-, 8th-, and 10th-order terms are -1×10^{-4}, 1.1813×10^{-5}, -2.2296×10^{-7}, and 1.4815×10^{-9}, respectively.

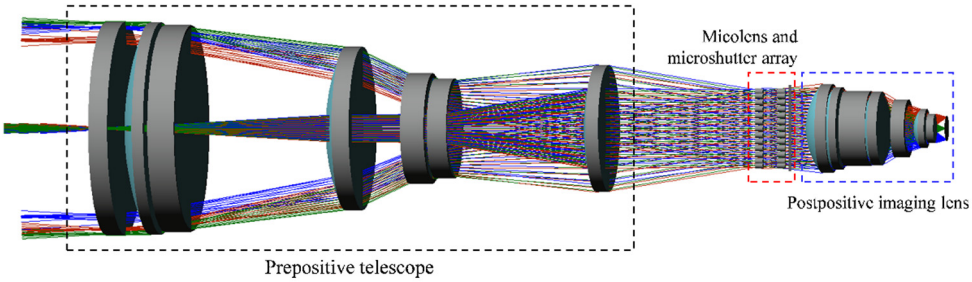


Figure 5. The optical path diagram of the designed FOV-gated optical imaging system.

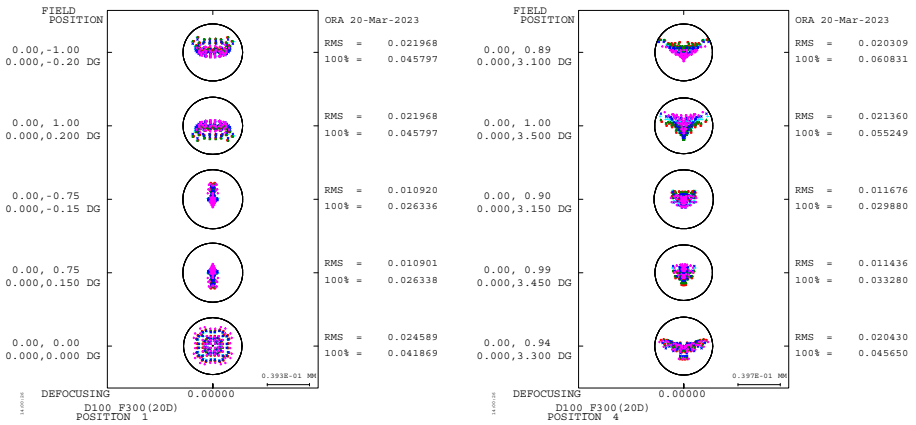
The imaging quality of the designed FOV-gated optical system is assessed through the analysis of spot diagrams and energy concentration. Figure 6a,b illustrate the spot diagrams of the stellar images within the central gated FOV (−0.2~0.2°) and the edge gated FOV (3.1~3.5°), respectively. The root mean square (RMS) radii of the spot diagrams for each gated FOV are all less than the Airy radius, indicating that near-diffraction-limited imaging is achieved across all gated FOVs.

The energy concentration can reflect the energy distribution of a stellar image on the detector, which has an essential influence on the SNR of a stellar image and can be evaluated by the encircled energy diagram. The encircled energy diagram illustrates the percentage of total energy enclosed as a function of the distance from the centroid of the stellar image. Figure 7a,b present the encircled energy diagrams in the central gated FOV (−0.2~0.2°) and the edge gated FOV (3.1~3.5°), respectively. In these diagrams, the abscissa denotes the distance from the centroid of the image spot, while the ordinate indicates the fraction of enclosed energy within the corresponding circle. As demonstrated in Figure 7a,b, the percentage of total energy enclosed within a 3 × 3 pixel area reaches 80% in both the

central gated FOV and the edge FOV, thereby satisfying the requirements for an all-time star sensor.

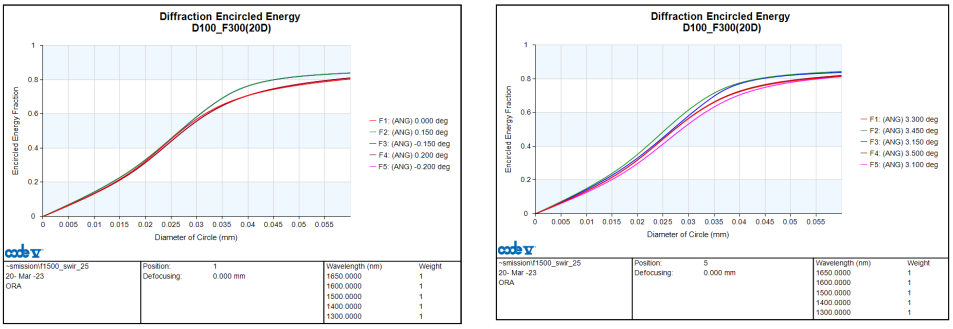
Table 3. The principal parameters of each optical element within the optical imaging system.

Surface Number	Surface Type	Radius	Thickness	Glass
1	Spherical	406.303	10.500	NSK16
2	Spherical	1255.309	0.1	
3	Spherical	104.934	24.000	HFK61
4	Spherical	−173.573	1.527	
5	Spherical	−159.427	7.000	NKZFS8
6	Spherical	718.894	37.337	
7	Spherical	126.030	16.000	HLAF3B
8	Spherical	−366.809	28.930	
9	Spherical	−146.808	6.500	HZF52
10	Spherical	205.762	2.262	
11	Spherical	1165.013	6.500	HZF52
12	Spherical	64.832	79.417	
13	Spherical	125.866	11.000	HZF52
14	Spherical	−387.870	73.400	
15	Spherical	Infinity	0.892	
16	Spherical	Infility	2.000	SILICA
17	Spherical	Infinity	2.000	NLAF2
18	Spherical	−6.795	6.525	
19	Spherical	Infinity	2.000	SILICA
20	Spherical	Infinity	2.000	NLAK21
21	Spherical	−9.048	10.000	
22	Spherical	35.580	6.800	NSF57
23	Spherical	49.072	0.100	
24	Spherical	40.346	10.000	NSF57
25	Spherical	358.495	4.795	
26	Spherical	−47.112	3.400	NSF4
27	Spherical	35.561	1.491	
28	Even aspheric	41.110	13.500	NLAF2
29	Spherical	−41.111	0.452	
30	Spherical	54.871	5.300	NSF57
31	Spherical	23.351	8.028	
32	Spherical	14.381	6.000	NSF57
33	Spherical	90.083	3.035	
34	Spherical	−11.167	2.200	ZNS
35	Spherical	−24.542	4.200	
36	Image plane			



(**a**) In the central gated FOV (−0.2~0.2°) (**b**) In the edge gated FOV (3.1~3.5°)

Figure 6. Spot diagrams of the stellar images in different gated FOVs.



(**a**) In the central gated FOV (−0.2~0.2°) (**b**) In the edge gated FOV (3.1~3.5°)

Figure 7. The energy concentration of the image spots in different gated FOVs.

5. Numerical Simulation

To validate the principle of suppressing sky background radiation and to assess the detection capabilities of the designed FOV-gated imaging system, a numerical simulation experiment was conducted utilizing stray light analysis software, ASAP 2011.

In accordance with the optical pathway of the FOV-gated optical imaging system, an optical–mechanical model of the designed optical system for an optical field analysis on the detector was established, as illustrated in Figure 8. By configuring the light source and conducting ray tracing, the illumination effects resulting from the stellar image and the background radiation from the sky on the detector are simulated. The simulation employs the Harvey Bidirectional Scattering Distribution Function (BSDF) Model, with the primary analysis conditions detailed in Table 4.

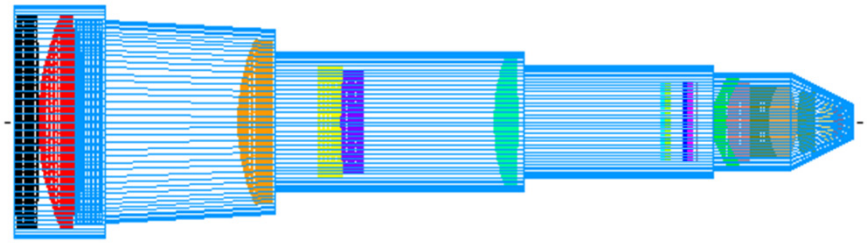


Figure 8. Optical–mechanical model of designed optical system for stray light analysis.

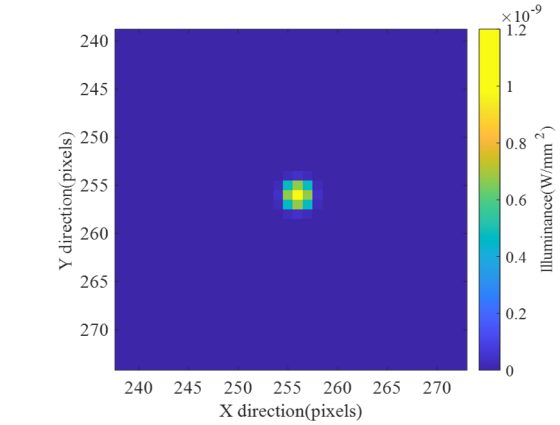
Table 4. Primary analysis conditions in the simulation.

Items	Parameter
Single-side transmittance of the optical element	99.5%
Residual reflectivity of the optical element	0.3%
Reflectivity of the microshutter array	3%
Surface roughness of optical parts	2 nm
Total integrated scattering (TIS) of structural parts	0.15
Light scattering times	2
Sampling number of the final image plane	511 × 511
Number of tracing rays	10 million

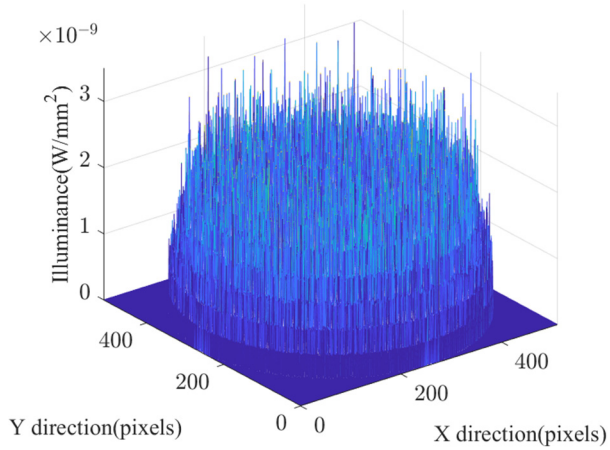
Two types of light sources were established for this study. The first light source, referred to as Light Source 1, represents the stellar signal, which consists of parallel light that uniformly illuminates the entire aperture of the optical system. As discussed in Section 3.1, the spectral irradiance of 0-magnitude stars in the H-band is quantified as 1.18×10^{-9} W/m^2·μm. Given that the effective aperture of the optical system measures 100 mm and the operational wavelength range spans 400 nm, the radiant flux entering the system is approximately 3.71×10^{-12} W. The second light source is the background radiation from the sky, which can be characterized as a surface source that adheres to Lambert's cosine law across the entire 2π steradian space. The analysis presented in Section 3.1

indicates that the typical radiant intensity at altitudes of 3 km is 0.35 W/m^2·Sr within the H-band. Taking into account the effective aperture of the optical system, which measures 100 mm, and the total FOV of 7°, the radiant flux entering the system is approximately 3.2×10^{-5} W.

Assuming that only the stellar signal from a 0-magnitude star enters the optical system at an incident angle of 0°, the central microshutter element is activated, and the gated instantaneous FOV ranging from −0.2° to 0.2° is gated. The illuminance produced by this stellar image on the detector is determined through simulation, as illustrated in Figure 9a. It is evident that the stellar image is predominantly concentrated within a 3 × 3 pixel area. The average illuminance across these 3 × 3 pixels is approximately 6.11×10^{-10} W/mm^2. In the same gated FOV, when only the sky background radiation with a radiant intensity of 0.35 W/m^2·Sr is allowed to enter the optical system, the calculated average illuminance on the detector is approximately 7.28×10^{-10} W/mm^2, as depicted in Figure 9b.



(**a**)



(**b**)

Figure 9. The illuminances generated by the stellar signal and the sky background radiation in the central gated FOV (−0.2~0.2°) on the detector simulated by the software ASAP. (**a**) The illuminance generated by a 0-magnitude star on the detector. (**b**) The illuminance produced by typical sky background radiation on the detector.

Similarly, an optical–mechanical model of a prepositive telescope imaging system, which includes only the prepositive telescope and the detector for an optical field analysis, was established. The primary analysis conditions in the simulation, as well as the light source settings, are consistent with those utilized in the simulation of the FOV-gated imaging system. The focal length of the prepositive telescope is measured at 300.83 mm, and the pixel dimension of the detector is 20 μm. Consequently, the FOV for a single pixel

is approximately 13.8 arcseconds. The detector is positioned 0.15 mm from the image plane of the prepositive telescope and is maintained in an out-of-focus state to ensure that the defocused stellar image encompasses a 3 × 3 pixel area.

Figure 10a illustrates the illuminance produced by a 0-magnitude star with a 0° incident angle on the out-of-focus detector of the prepositive telescope imaging system, as determined through simulation. It is evident that the stellar image is distributed across a 3 × 3 pixel array, with an average illuminance value of approximately 6.96×10^{-10} W/mm^2. Figure 10b depicts the illuminance resulting from sky background radiation, characterized by a radiant intensity of 0.35 W/m^2·Sr, on the out-of-focus detector. The average illumination value on the detector is found to be approximately 2.13×10^{-8} W/mm^2.

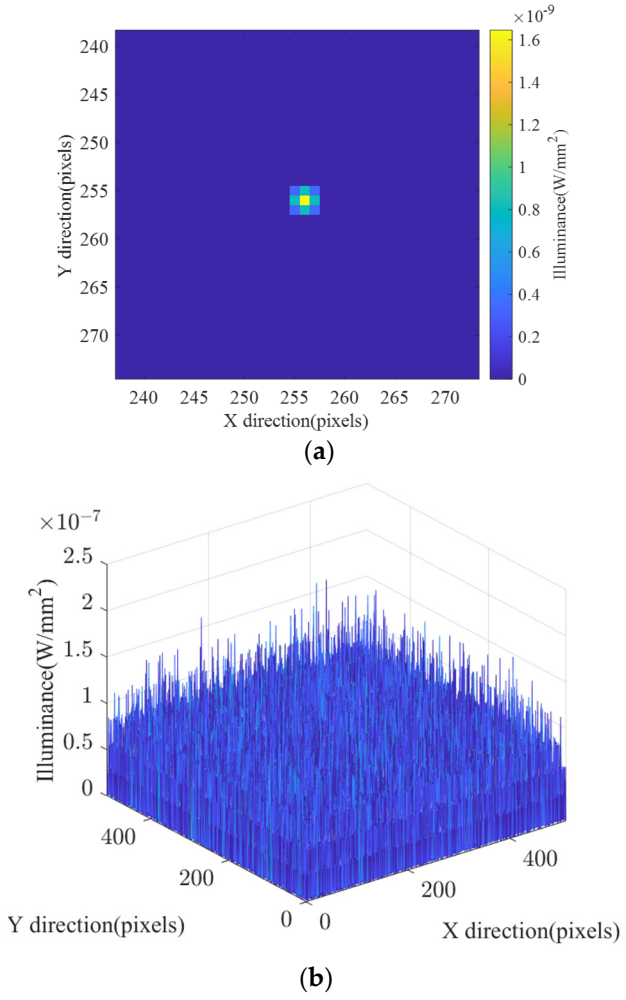


Figure 10. The illuminances generated by the stellar signal and the sky background radiation on the out-of-focus detector in the prepositive telescope imaging system simulated by the software ASAP. (**a**) The illuminance generated by a 0-magnitude star with a 0° incident angle. (**b**) The illuminance produced by typical sky background radiation.

In comparison to the designed FOV-gated optical imaging system, the average illuminance attributed to the stellar signal across a 3 × 3 pixel array in the prepositive telescope imaging system exhibits a slight increase due to enhanced transmittance. However, the average illuminance resulting from typical sky background radiation demonstrates a significant increase. It can be observed that the ratio of illuminance from the stellar signal to that from the sky background radiation in a single pixel of the FOV-gated optical imaging system is approximately 25 times greater than that in the prepositive telescope imaging system. This finding aligns with the theoretical analysis presented in Section 2, which

indicates that the magnification factor (n) of the imaging in the FOV-gated optical imaging system is approximately 5.

6. Discussion

It is noted that the ASAP software is limited to calculating the illuminances produced by stellar signals and sky background radiation; it does not compute the SNR of the stellar imaging on the detector. To assess the SNR and the detectable limiting magnitude, it is essential to calculate the number of electrons generated by these simulated illuminances.

If the average illuminance value of a stellar image with a magnitude of 0 is determined on the detector, the corresponding number of electrons generated by the stellar signal in a pixel can be expressed as follows:

$$S_{p0} = K_0 S_0 = E_{s0} d_{pixel}^2 t \frac{Q_0(\lambda)}{h\nu} \tag{20}$$

In a similar manner, if the average illuminance of the sky background radiation incident on the detector is quantified, the resultant number of electrons generated by the sky background radiation within a pixel can be expressed as follows:

$$B = E_b d_{pixel}^2 t \frac{Q_0(\lambda)}{h\nu} \tag{21}$$

From the simulation results, the average values of the illuminance E_{s0} and E_b for the proposed FOV-gated optical imaging system are 6.11×10^{-10} W/mm^2 and 7.28×10^{-10} W/mm^2, respectively. On the other hand, the prepositive telescope optical imaging system containing only the prepositive telescope and detector can be regarded as a traditional star sensor optical system with 100 mm aperture, 300.8 mm focal length, and 2° FOV. The average values of the illuminance E_{s0} and E_b for the traditional star sensor optical system are, respectively, 6.96×10^{-10} W/mm^2 and 2.13×10^{-8} W/mm^2. Based on these illumination values, the detectable limiting magnitude of both the designed FOV-gated optical imaging system and the constructed traditional star sensor optical system under varying exposure times can be assessed according to Equations (18)–(21), as illustrated in Figure 11.

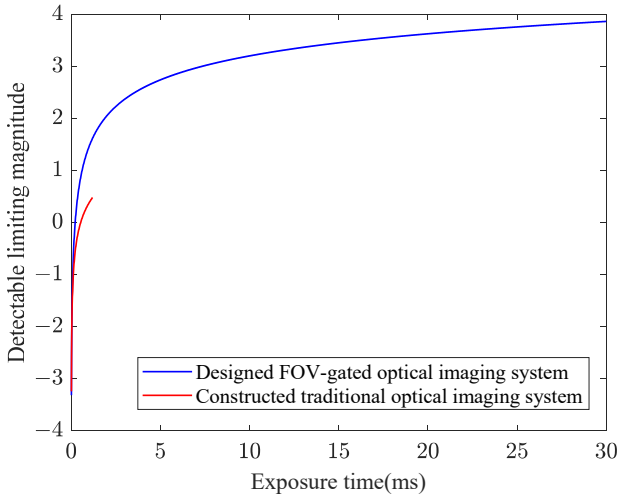


Figure 11. The detectable limiting magnitude of the designed gated FOV optical imaging system, as well as that of the constructed traditional star sensor optical system, was evaluated based on the illumination derived from numerical simulations.

It can be seen from the blue curve in Figure 11 that the maximum exposure time of the designed gated FOV optical imaging system can reach 30 ms, allowing for the detection of nearly 3.9 magnitudes in the H-band under typical daytime sky background radiation. This

finding is consistent with the theoretical analysis presented in Section 3.2. Given that the total FOV of the designed optical system is 7°, an FOV duty cycle greater than 0.6 results in an effective total FOV of 4.2°. Consequently, the probability of detecting at least three stars exceeds 80%, as illustrated in Figure 4. In contrast, the maximum exposure time of the constructed traditional star sensor optical system is limited to only 1.2 ms, with a detectable limiting magnitude of merely 0.5 in the H-band, as indicated by the red curve in Figure 11. In this scenario, the probability of detecting three stars within a 2° FOV is nearly zero.

Based on the discussion above, it is evident that traditional optical imaging systems are characterized by a singular FOV. The size of the FOV is constrained by the capacity to mitigate sky background radiation. As the FOV increases, it is theoretically possible to observe a greater number of stars; however, this also results in an increase in sky background radiation, which may diminish detection capabilities. FOV-gated optical imaging systems are characterized by two distinct FOVs: the gated FOV, which plays a crucial role in suppressing sky background radiation and influences the detectable limiting magnitude, and the total FOV, which primarily determines the observational scope for detecting stars. A narrow gated FOV combined with a wide total FOV is advantageous for enhancing the probability of multi-star detection during the daytime.

In practical applications, several issues require further resolution. During the processing and assembly of an FOV-gated optical imaging system, the optical parameters associated with each gated FOV may not exhibit complete consistency. To attain high-precision detection, it is essential to calibrate the optical parameters both within and between the gated FOVs, as well as to achieve the high-precision reconstruction of the relative positions of multiple star spots. Moreover, there is a need to investigate new algorithms that facilitate the high-precision extraction of star spot positions on dynamic platforms under bright background conditions. Additionally, optimizing the optical system is crucial to enhance the duty cycle of the gated FOV corresponding to the microlens element, thereby expanding the effective FOV of the system and increasing the probability of multi-star detection.

The FOV-gated optical imaging system is mainly designed for detecting multiple stars in the atmosphere during the daytime. For applications outside the atmosphere, such as on satellite platforms, the FOV-gated optical imaging system generally presents few apparent advantages. Additionally, the system is characterized by a complex structure and high costs due to integrating microlens and the microshutter array. Nevertheless, the system's long focal length and high angular resolution can provide certain benefits for satellite platforms, particularly in achieving high-precision attitude measurements.

7. Conclusions

This study presents the principles underlying the suppression of sky background radiation in an FOV-gated optical imaging system, based on its imaging characteristics. The analysis focuses on applications involving airborne platforms operating at altitudes of 3 km and above, examining the detectable stellar magnitude limit and the detection probability of the FOV-gated imaging system under typical sky background radiation conditions. An FOV-gated imaging system was designed with a working wavelength range of 1.3 μm to 1.7 μm, a 100 mm aperture, a focal length of 1489 mm, a gated FOV of 0.4°, and a total FOV of 7°. The stray light analysis software ASAP was utilized to simulate the illuminance resulting from stellar light and sky background radiation on the detector. The simulation results demonstrate the effectiveness of the FOV-gated imaging system in suppressing sky background radiation, allowing for the estimation of the detectable stellar magnitude limit of the designed optical system. The findings align with theoretical calculations, indicating that the detectable limiting stellar magnitude can reach approximately 3.9 in the H-band with a 30 ms exposure time. Furthermore, the probability of detecting at least three stars exceeds 80% within a total FOV of 4.2° during daytime conditions. This research provides a viable technical approach for achieving multi-star detection and star pattern recognition in daylight, thereby facilitating the autonomy of all-time star sensors.

Author Contributions: Conceptualization, L.F.; methodology, L.F. and H.Z.; software, H.Z. and X.C.; validation, L.F. and X.C.; formal analysis, L.F. and Z.F.; investigation, Z.L. and Z.F.; resources, Q.Z. and R.Z.; data curation, L.F. and Z.F.; writing—original draft preparation, L.F.; writing—review and editing, H.Z.; visualization, L.F.; project administration, L.F.; funding acquisition, L.F., Q.Z. and R.Z. All authors have read and agreed to the published version of the manuscript.

Funding: This research was funded by the National Key Research and Development Program of China, grant number 2019YFA0706001; Sichuan Outstanding Youth Science and Technology Talent Project (2022JDJQ0027); and Sichuan Science and Technology Program (Grant No. 2024NSFSC1443 and No. 2024YFHZ0030).

Institutional Review Board Statement: Not applicable.

Informed Consent Statement: Not applicable.

Data Availability Statement: The data presented in this study are available from the corresponding author upon reasonable request.

Conflicts of Interest: The authors declare no conflicts of interest.

References

1. Liebe, C.C. Accuracy performance of star trackers—A tutorial. *IEEE Trans. Aerosp. Electron. Syst.* **2002**, *38*, 587–599. [CrossRef]
2. Zhao, Y.; Wei, X.; Li, J.; Wang, G. Star identification algorithm based on K-L transformation and star walk formation. *IEEE Sens. J.* **2016**, *16*, 5202–5210. [CrossRef]
3. Wei, X.; Cui, C.; Wang, G.; Wan, X. Autonomous positioning utilizing star sensor and inclinometer. *Measurement* **2019**, *131*, 132–142. [CrossRef]
4. Zhou, Y.; Shen, W. Conceptual design of airborne daytime infrared star cameras. *Proc. SPIE* **2010**, *7849*, 217–225.
5. Dietz, K.L.; Ramsey, B.D.; Alexander, C.D.; Apple, J.A.; Ghosh, K.; Swift, R.W. Daytime aspect camera for balloon altitudes. *Opt. Eng.* **2001**, *41*, 2641–2651. [CrossRef]
6. Alexander, C.D.; Swift, W.R.; Ghosh, K.; Ramsey, B.D. Design of a Day/Night Star Camera System. *Proc. SPIE* **1999**, *3779*, 47–54.
7. Wang, W.; Wei, X.; Li, J.; Zhang, G. Guide star catalog generation for shortwave infrared (SWIR) All-Time star sensor. *Rev. Sci. Instrum.* **2018**, *89*, 075003. [CrossRef] [PubMed]
8. Wu, L.; Xu, Q.; Wang, H.; Lyu, H.; Li, K. Guide Star Selection for the Three-FOV Daytime Star Sensor. *Sensors* **2019**, *19*, 1457. [CrossRef] [PubMed]
9. Zhang, H.; Zhou, X.D.; Wang, X.M.; Tian, H. A survey of technology status and development of all-day star sensor in near-earth space. *Acta Aeronaut. Astronaut. Sin.* **2020**, *41*, 623719.
10. Whitman, R.B. *Astroinertial Navigation for Cruise Applications*; Northrop Corporation Electronics Division: Hawthorne, CA, USA, 2008.
11. Lewis, S.W.; Hockbruckner, M.; Reeve, J. Stellar Inertial navigation growing with the times upgrading of the LN-20 integrated inertial navigation system. In Proceedings of the 1991 National Technical Meeting of The Institute of Navigation, Phoenix, AZ, USA, 22–24 January 1991; pp. 295–302.
12. Belenkii, M.; Bruns, D.G.; Rye, V.A.; Bringkley, T. Daytime Stellar Imager. US7349803B2, 25 March 2008.
13. Fang, L.; Liu, E.; Zhang, H.; Wei, X.; Cheng, X.; Liao, Z.; Zhao, R. Optical imaging system for an all-time star sensor based on field of view gated technology. *Appl. Opt.* **2022**, *61*, 5859–5868. [CrossRef] [PubMed]
14. Fang, L.; Wang, W.; Wang, Q.; Tan, S.; Zhang, H.; Zhao, R.; Liu, E. An Electromagnetic-Driven Microshutter Array in a Field-of-View Gated Image System for All-Time Star Sensors. *Micromachines* **2023**, *14*, 452. [CrossRef] [PubMed]
15. Wang, W.; Wei, X.; Li, J.; Du, J.; Zhang, G. Optical Parameters Optimization for All-Time Star Sensor. *Sensors* **2019**, *19*, 2960. [CrossRef] [PubMed]
16. Wu, L.; Wang, J.L.; Wang, H.J. Guide star selection for star pattern recognition between three FOVs. *Opt. Precis. Eng.* **2015**, *23*, 1732–1741.
17. Wang, W.; Wei, X.; Li, J.; Wang, G. Noise suppression algorithm of shortwave infrared star image for daytime star sensor. *Infrared Phys. Technol.* **2017**, *85*, 382–394. [CrossRef]
18. Martin, V.Z. *Handbook of Space Astronomy and Astrophysics*, 2nd ed.; Cambridge University Press: New York, NY, USA, 2003.
19. Chen, L.; Yan, G.; Wang, T.; Ren, H.; Calbó, J.; Zhao, J.; McKenzie, R. Estimation of surface shortwave radiation components under all sky conditions: Modeling and sensitivity analysis. *Remote Sens. Environ.* **2012**, *123*, 457–469. [CrossRef]

Disclaimer/Publisher's Note: The statements, opinions and data contained in all publications are solely those of the individual author(s) and contributor(s) and not of MDPI and/or the editor(s). MDPI and/or the editor(s) disclaim responsibility for any injury to people or property resulting from any ideas, methods, instructions or products referred to in the content.